

## 1.1 Initial scientific uses of coherent synchrotron radiation in electron storage rings

D.N. Basov<sup>4</sup>, J. Feikes<sup>1</sup>, D. Fried<sup>5</sup>, K. Holldack<sup>1</sup>, H.W. Hübers<sup>2</sup>, P. Kuske<sup>1</sup>, M.C. Martin<sup>3</sup>,  
S. G. Pavlov<sup>2</sup>, U. Schade<sup>1</sup>, E.J. Singley<sup>3</sup>, G. Wüstefeld<sup>1</sup>

<sup>1</sup>Berliner Elektronenspeicherring-Gesellschaft für Synchrotronstrahlung m.b.H.,  
Albert-Einstein-Straße 15, 12489 Berlin, Germany

<sup>2</sup>German Aerospace Center, Institut for Planetary Research,  
Rutherford-Straße 2, 12489 Berlin, Germany

<sup>3</sup>Advanced Light Source Division, Lawrence Berkeley National Laboratory,  
1 Cyclotron Road, Berkeley, California 94720, USA

<sup>4</sup>Department of Physics, University of California, San Diego,  
9500 Gilman Drive, La Jolla, California, 92093, USA

<sup>5</sup>Division Biomaterials and Bioengineering, Department of Preventive and Restorative Dental  
Sciences, University of California, San Francisco, 707 Parnassus Ave., San Francisco,  
California, 94143-0758, USA

mail to: [schade@bessy.de](mailto:schade@bessy.de)

### 1.1.1 Introduction

The terahertz (THz) and sub-THz region of the electromagnetic spectrum bridges the infrared and the microwave. This boundary region is beyond the normal reach of optical and electronic measurement techniques normally associated with these better-known neighbors. Only over the past decade has this THz region become scientifically accessible with broadband sources of moderate intensity being produced by ultra-fast laser pulses incident on biased semiconductors or non-linear crystals [1, 2]. Very recently, a much higher power source of THz radiation was demonstrated: coherent synchrotron radiation (CSR) from short, relativistic electron bunches [3-5]. Coherent synchrotron radiation will open up new territory in the THz frequency range with intensities many orders of magnitude higher than previous sources. The energy range between microwave and the far infrared,  $3 - 33 \text{ cm}^{-1}$  ( $0.1 - 1 \text{ THz}$ ), has proven to be challenging to access and is therefore referred to as the “THz gap”. However, with the new CSR source at BESSY [3, 5] we have been able to extend traditional infrared measurements down into this sub-terahertz frequency range. This source is broadband and is made up of longitudinally coherent single-cycle sub-picosecond pulses with a high repetition rate (100’s of MHz). With the combination of high intensity and short pulse duration new opportunities for scientific research and applications are enabled across a diverse array of disciplines from condensed matter physics, to medical, technological, manufacturing, space and defense industries. Imaging, spectroscopy, femtosecond dynamics, and driving novel non-linear processes are all among the potential applications. The high average power of the CSR source allows one to extend experimental conditions to lower frequencies than have been possible with thermal and conventional synchrotron sources

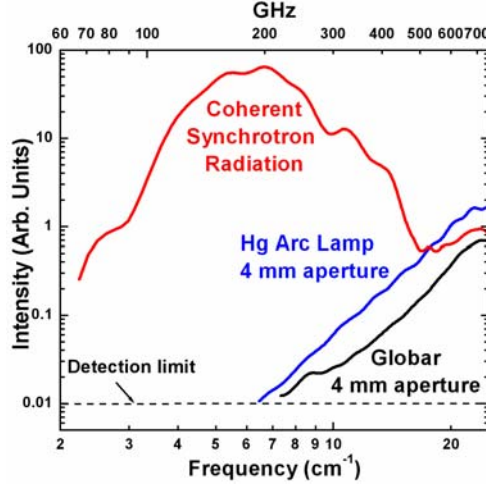


**Figure 1:** Measured far-IR intensity for the BESSY CSR source, compared to mercury arc and tungsten conventional thermal sources. While the turn-on of the CSR source below  $2\text{ cm}^{-1}$  is a real effect of the CSR emission process, the drop off at the low frequency end is due to a combination of diffraction losses in the optical path of the beamline and the cutoffs of the optical components, such as the mylar beamsplitter, in the interferometer.

(Figure 1). In this paper, we make use of the stable CSR THz source at BESSY for three initial scientific demonstration experiments.

The coherent synchrotron radiation at BESSY was used to precisely measure transitions of singly ionized shallow acceptors in semiconductors by means of photoconductive spectroscopy. As a prototype material for these experiments germanium doped by gallium (Ge:Ga) was used. Ge:Ga is a widely used detector material for applications at terahertz frequencies. Detectors of this system have for instance been used onboard of ISO [6], ESA's Infrared Space Observatory, and are currently in use in NASA's Spitzer space telescope. A thorough understanding of the detector response is of prime importance for the interpretation of the data measured with these expensive instruments. THz CSR provides a powerful tool to characterize the response of these detectors as well as to investigate the physical mechanisms involved in the detection process. The results obtained at BESSY allow to identify the origin of a long wavelength ( $> 300\text{ }\mu\text{m}$ ) response. It can be attributed to transitions from excited Ga states into the valence band. The results indicate that a cascade type of relaxation exists in Ge:Ga at 4.5 K.

In another experiment at BESSY we used the high brilliance of the CSR for optical reflectivity measurements of the c-axis Josephson plasma resonance (JPR) in the highly anisotropic, optimally doped high-temperature superconductor  $\text{Bi}_2\text{Sr}_2\text{CaCu}_2\text{O}_8$  at low frequencies [7] which is not reachable by conventional sources for optical measurement on high-temperature superconductors. Despite being perhaps the most frequently studied high- $T_c$  compound, the JPR, which is a direct probe of the superfluid density, has until now not been observed due to its frequency being lower than can be reached by traditional optical spectroscopy systems. In the particular experiment we obtain the magnitude and temperature dependence of the Josephson plasma frequency in zero magnetic field.

The high brilliance of this new accelerator-based coherent source at BESSY is also employed for scanning near-field microscopy in the THz and sub-THz range where spatial resolution below the diffraction limit is achieved [8]. Together with a Martin-Puplett spectrometer this technique enables spectroscopic mapping of samples under investigation. The potential of the technique is exemplified by images of biological samples. Strongly absorbing living leaves have been imaged in transmittance with a spatial resolution of  $130\text{ }\mu\text{m}$

at about 12 wavenumbers (0.36 THz). The THz near-field images reveal distinct structural differences of leaves from different plants investigated. The CSR source can also be used for spectral imaging of bulky organic tissues. Human teeth samples of various thicknesses have been imaged between 2 and 20 wavenumbers (between 0.06 and 0.6 THz). Regions of enamel and dentin within tooth samples are spatially and spectrally resolved, and buried caries lesions are imaged through both the outer enamel and into the underlying dentin.

### 1.1.2 Sub-terahertz response of stressed and unstressed Ge:Ga photoconductive detectors

Germanium doped with gallium (Ge:Ga) is widely used for sensitive detectors of far-infrared (FIR) or terahertz (THz) radiation [9]. The detection mechanism is based on a transition from the Ga ground state to the valence band. The long-wavelength cutoff of such detectors is determined by the energy of the ground state, for Ge:Ga  $\sim 120 \mu\text{m}$  [10]. This cutoff can be extended to longer wavelengths ( $\sim 240 \mu\text{m}$ ) by applying a compressive force to the crystal [11]. A compressive force along the  $\langle 100 \rangle$  crystal axis removes the degeneracy at the top of the valence band and decreases the acceptor binding energy [12]. Detectors of this type are utilized in many space or airborne observatories for far-infrared astronomy. Examples are ISO, ESA's Infrared Space Observatory [6], the Spitzer Space Telescope [13], which is currently in operation, and SOFIA, the Stratospheric Observatory for Infrared Astronomy, a DLR-NASA observatory [14]. Despite the wide use of this type of detector there remain some fundamental questions: A long wavelength response at  $1\text{-}10 \text{ cm}^{-1}$  which increases with applied stress was observed by several groups in unstressed Ge:Ga [15, 16]. However the origin of the response remained unclear. Another peculiarity of Ge:Ga, which is controversially discussed is, whether the cascade capture model is the appropriate explanation for hole capture by attractive hydrogen centers such as Ga in p-type germanium [17]. It has been proposed that direct capture into the ground state exceeds cascade capture for  $T > 3 \text{ K}$  for singly ionized acceptors [18, 19].

The experiments have been performed at the THz port of the IRIS beamline [20] at BESSY using a polarizing step scan Fourier transform spectrometer (FTS) [21]. Single sided interferograms have been measured. The unapodized resolution was  $0.15 \text{ cm}^{-1}$ . BESSY was operated in a dedicated low  $\alpha$  mode ( $\alpha = 4 \times 10^{-5}$ ) with a current of about 40 mA. In this way powerful and coherent THz synchrotron (CSR) radiation below  $50 \text{ cm}^{-1}$  was generated [3, 5]. The unstressed Ge:Ga is a cube of 4 mm side length with a doping concentration of  $6 \times 10^{15} \text{ cm}^{-3}$  and a compensation of about 1%. The stressed Ge:Ga is a cube of  $1 \times 1 \times 1 \text{ mm}^3$  with a Ga doping concentration of  $2 \times 10^{14} \text{ cm}^{-3}$  and a compensation of less than 1%. Stress was applied by a screw and a piston. A ball bearing decoupled the torque from the screw from the detector. By this means a compressive force of  $\sim 6 \times 10^8 \text{ Pa}$  was applied along the  $\langle 100 \rangle$  crystal axis. The samples were mounted in a liquid Helium cryostat. The temperature of the samples was 4.5 K. A cold black polyethylene filter was mounted in front of the samples to reduce background radiation. The THz CSR radiation from BESSY passed through the FTS and was concentrated onto the samples by a parabolic mirror and a cone. The photocurrent induced by the CSR in the samples was detected by a lock-in amplifier with reference to the 1.25 MHz revolution frequency of BESSY.

A typical interferogram is shown in Fig. 2 while Fig. 3 displays the photoconductivity spectra for stressed and unstressed Ge:Ga. The upper trace in Fig. 3 is the spectrum of unstressed Ge:Ga. The two peaks between 4 meV and 6 meV are due to the Sb donors, which are the compensating dopants in Ge:Ga. The larger peak at 5.72 meV corresponds to the transition from the  $1s(A_1)$  ground state to the  $2p_0$  state (5.71 meV [22, 23]) and the smaller peak at 4.82 meV to the transition from the  $2p_0$  state to the conduction band (4.74 meV [22,

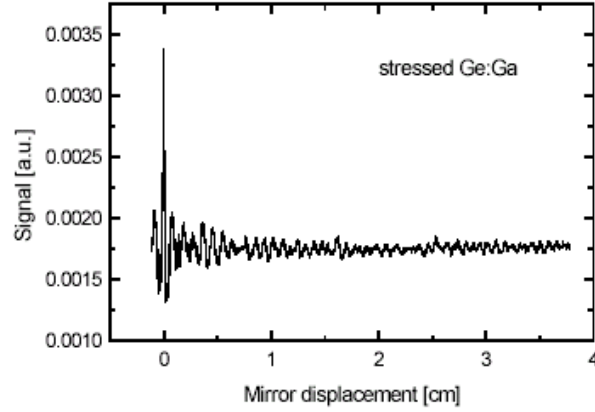


**Figure 2:** Interferogram obtained from the stressed Ge:Ga crystal.

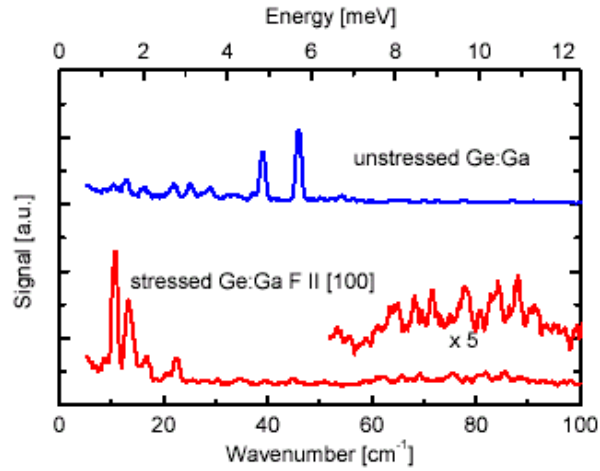


**Figure 3:** Photoconductivity spectra of unstressed and stressed Ge:Ga.

23]). The small peaks below 3 meV are due to transitions from bound excited states of Ga to the valence band.

The stressed Ge:Ga shows a broad response between 6 and 10 meV due to the transition from the ground state to the valence band. This is the spectral range for which the detector is made. However, there is a strong response below about 2 meV. Again, this is due to transitions from bound excited states of Ga to the valence states (Fig. 3). It is important to note that the data are not calibrated for the CSR spectrum. Therefore, the relative intensities are arbitrary. The population of the excited states is due to the peculiarities of the de-excitation process after a hole is excited into the valence band by the powerful CSR. Direct capture into the ground state can not be the only path for de-excitation because absorption on excited states is observed. The spectra indicate that capture into at least some of the excited states takes place.

The results show a significant response of Ge:Ga detectors at long wavelengths outside the bands for which they are originally designed. For any detector application care should be taken to block the long wavelength response by appropriate filters. In addition, the results

indicate that a cascade type of relaxation exists in Ge:Ga at 4.5 K. In case of direct capture to the ground state none of the excited states would be observable.

### 1.1.3 Observation of the Josephson plasma resonance in optimally doped $\text{Bi}_2\text{Sr}_2\text{CaCu}_2\text{O}_{8-\delta}$

One of the most outstanding problems in the field of high temperature superconductivity is determining how the normal state quasi-2D metal is related to the 3D superconducting state. For all cuprate superconductors the gross electronic properties within the  $\text{CuO}_2$  planes are similar, exhibiting a “bad metal” behavior. The carrier concentration is low and the damping is strong. In contrast, the electronic properties perpendicular to the  $\text{CuO}_2$  planes cover a broad spectrum, from marginally conducting overdoped  $\text{YBa}_2\text{Cu}_3\text{O}_7$ , to the essentially insulating character of  $\text{Bi}_2\text{Sr}_2\text{CaCu}_2\text{O}_8$ . The role of this varying degree of anisotropy in the  $\text{CuO}_2$  intralayer and interlayer electronic properties in producing high temperature superconductivity is still unresolved [24].

The energy scale of the Josephson plasma edge is directly related to the degree of anisotropy of the material. In nearly all families of high temperature superconductors the plasma edge has been observed in the far infrared frequency range [25]. The one exception is in the extremely anisotropic  $\text{Bi}_2\text{Sr}_2\text{CaCu}_2\text{O}_8$  (Fig. 4, left) where at optimal doping the plasma edge has not been seen. By doping this compound with Pb, and hence lowering the anisotropy (and  $T_c$ ), the plasma edge is observed near  $40 \text{ cm}^{-1}$  [26]. Additionally, when reducing the carrier doping a resonance is observed in magnetoabsorption experiments in the microwave region, usually attributed to the Josephson plasma effect [27]. Our reflectivity measurements on optimally doped  $\text{Bi}_2\text{Sr}_2\text{CaCu}_2\text{O}_8$  down to  $4 \text{ cm}^{-1}$  using the coherent synchrotron radiation at BESSY show the Josephson plasma resonance, clearly.

In order to make specular reflectance measurements at wavelengths in excess of 1 mm, it is necessary to have a sample larger than the wavelength of the probing radiation. Since single crystal of high temperature superconductors with c-axis dimension  $\gg 1 \text{ mm}$  are difficult to prepare, a mosaic of several pieces of a crystal was assembled with a net c-axis length of  $\sim 5 \text{ mm}$  (Fig. 4, right). While this circumvents problems of diffraction effects, additional

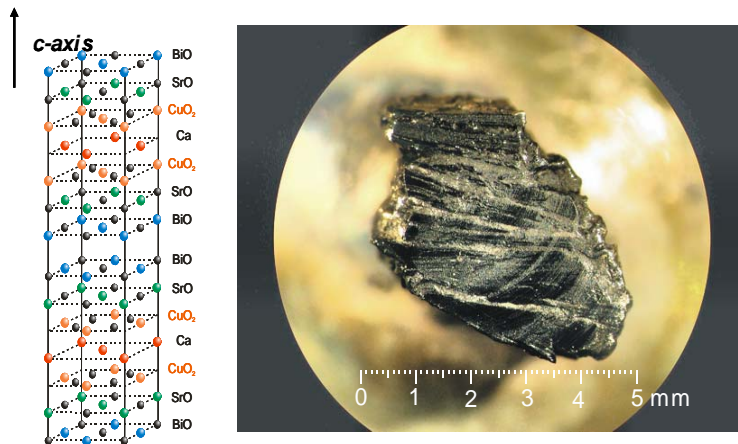


**Figure 4:** Structure of  $\text{Bi}_2\text{Sr}_2\text{CaCu}_2\text{O}_8$  (left) and the mosaic of the single crystals used in this investigation (right). To account the contribution to the measured reflectance the area of epoxy showing was estimated and the experimental reflectance was corrected accordingly.

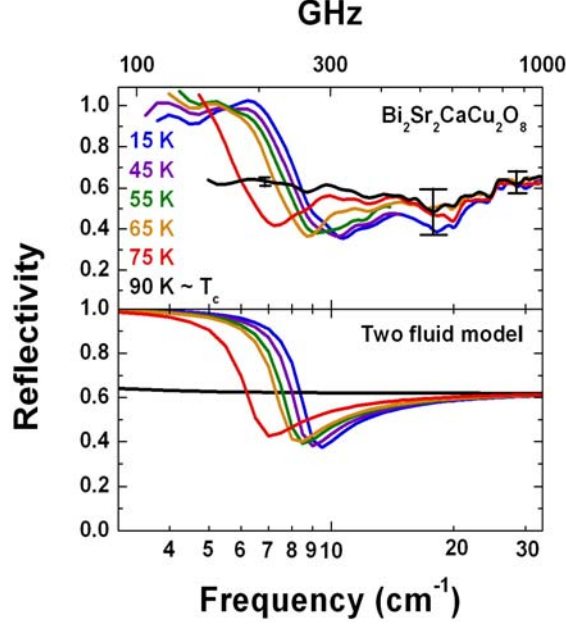


**Figure 5:** Measured c-axis polarized near-normal reflectivity of  $\text{Bi}_2\text{Sr}_2\text{CaCu}_2\text{O}_8$  (upper panel) for various temperatures at or below the superconducting transition temperature,  $T_c$ . A resonance that shifts with temperature and disappears above  $T_c$  is clearly observed. The lower panel shows the calculated reflectivity of a superconductor with a shifting Josephson Plasma Resonance.

complications arise due to reflection from the conducting epoxy that binds the individual crystals together. Absolute values of the reflectivity were obtained by coating the sample in situ with a thin layer of gold, and using the gold coated sample as a reference.

The top panel of Fig. 5 shows the experimental reflectance in the sub-terahertz region on a logarithmic frequency scale. It is useful to examine the normal state spectrum at 90 K (black curve) to discuss the signal to noise ratio in different frequency regions. On the high energy side of the spectrum the signal to noise is  $\pm 5\%$ . This is due to the relatively low intensity of the source at these energies (Fig. 1). The largest noise contribution is in a small band near  $20\text{cm}^{-1}$ , where the uncertainty is now  $\pm 10\%$ . This is 50 Hz electrical noise in the synchrotron electron beam and/or the beamline. The Fourier transform interferometer modulates this to the frequency range near  $20\text{ cm}^{-1}$ . Most significant is the relatively small error of  $\pm 2\%$  in the very low frequency range. Hence, the best response of the CSR measurement system is at the most inaccessible region for traditional infrared sources.

In contrast to the nearly flat and featureless spectrum at  $T = T_c$ , the  $R(\omega)$  spectra at  $T < T_c$  show a strong  $\omega$  dependence. Below  $T_c$  the spectrum has a shallow minimum followed by a strong rise in the reflectivity. At the lowest frequency the spectra saturate to a constant value near unity. As the temperature decreases while the sample is in the superconducting state, both the minimum and reflectance edge increase in frequency, although this shift nearly saturates by 15 K. The reflectance edge in the superconducting state signals the flow of supercurrents along the c-axis. Since the density of superfluid increases as the temperature is lowered, the reflectance edge shifts to higher frequencies.

In order to extract quantitative information from the spectrum we model the reflectance with a two fluid model. One component consists of the dissipationless supercurrents, while the other is an over-damped plasmon [28]. The second term is necessary to account for finite reflectivity at the plasma minimum, and the rounding at the top of the reflectance edge. The

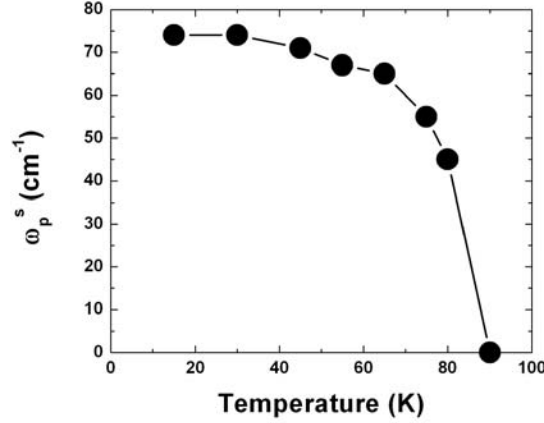


**Figure 6:** Superfluid plasma frequency as a function of temperature. Plasma frequency was determined from fitting the reflectance spectra with the two fluid model shown in the bottom panel of Figure 5.

bottom panel of Fig. 5 shows the results of this modeling. The magnitude, the frequency and the temperature dependence of the data in the top panel are well accounted for.

Using the above modeling we are also able to extract the value of the unscreened Josephson plasma frequency. At 15 K we obtain a value of  $\omega_{ps} = 74 \text{ cm}^{-1}$ . This value corresponds to a c-axis penetration depth value of  $\lambda_c = 21 \text{ }\mu\text{m}$ . The complete temperature dependence of the Josephson plasma frequency is summarized in Fig. 6. The plasma frequency rises quickly below  $T_c$ , and is nearly saturated at the low temperature limit by  $T_c/2$ .

Another dip in our experimental data near  $20 \text{ cm}^{-1}$  might be a transverse Josephson plasma mode [29] in  $\text{Bi}_2\text{Sr}_2\text{CaCu}_2\text{O}_8$  caused by the two different distances between CuO layers in the crystal structure. This feature in the data is, however, located right where the signal to noise ratio is the worst due to interference from 50 Hz pickups. This will be investigated further.

We report here the directly measured the Josephson plasma resonance in optimally doped  $\text{Bi}_2\text{Sr}_2\text{CaCu}_2\text{O}_8$  for the first time by applying the powerful coherent synchrotron radiation source at BESSY. The results presented provide a connection between the magnetoabsorption experiments performed on underdoped  $\text{Bi}_2\text{Sr}_2\text{CaCu}_2\text{O}_8$  and the infrared experiments in other families of high temperature superconductors.

#### 1.1.4 THz scanning near-field microspectroscopy on biological samples

The spatial resolution of conventional THz imaging is diffraction limited and thus only features with a dimension from hundred micrometers to millimeters are resolvable. This limit can be overcome by utilizing near-field imaging techniques [30] achieving spatial resolutions of up to  $\lambda/1000$  [31]. However, extremely brilliant sources are necessary to compensate for intensity losses to confine the THz radiation at the cost of total power.

A THz scanning near-field imaging (SNIM) technique benefiting from the broadband and highly brilliant coherent synchrotron radiation (CSR) from an electron storage ring [3, 5] is established at BESSY utilizing a detection method based on locking onto the intrinsic time structure of the synchrotron radiation. The CSR source at BESSY is a pulsed source with a frequency of 1.25 MHz determined by the time the relativistic electron bunch needs to travel one orbit with a circumference of 240 m. The emitted CSR power varies with the square of



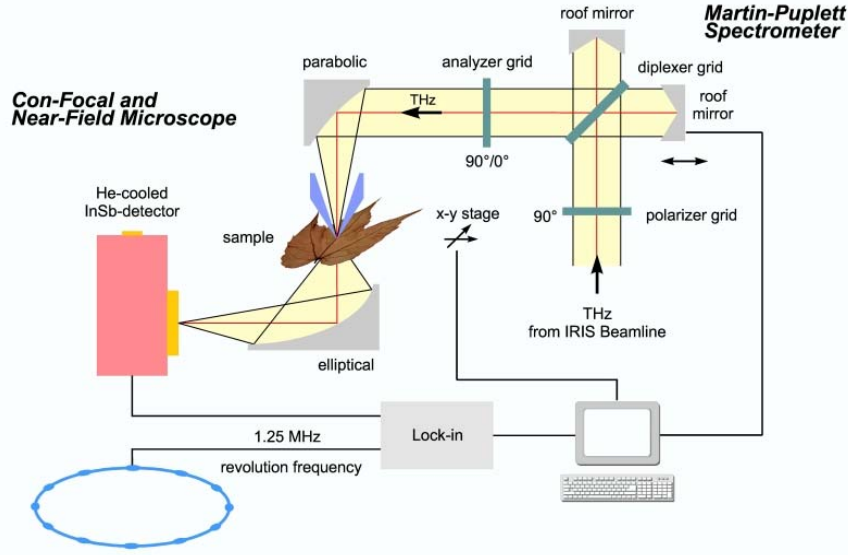


**Figure 7:** Schematic diagram of the THz scanning near-field infrared microscopy (SNIM) setup.

the decaying electron ring current stored which has to be taken into account for data normalization.

The THz SNIM is attached to the infrared beamline IRIS [20] at BESSY and the setup is shown in Fig. 7. The far-infrared port of the beamline provides a collimated CSR THz beam which is about 98% linearly polarized. The THz beam passes through a Martin-Puplett spectrometer before being transferred to the SNIM where it is focused into a conical waveguide with a circular cross-section and an exit aperture of a diameter smaller than the wavelength. The sample is held in front of the exit aperture by a spring ensuring that the sample is in direct contact to the probe. Imaging is performed by moving the sample in front of the exit aperture by means of a computer controlled x-y stage. The evanescent field at the exit aperture penetrates the sample and the scattered radiation containing the spectral information is collected by an ellipsoidal mirror and is then focused onto a LHe-cooled InSb detector. The revolution frequency of the electron bunches stored is used as a reference for lock-in detection of the SNIM signal by a fast liquid He cooled InSb detector. This detection provides a detection dynamics of nine orders of magnitude, which is essential for near-field

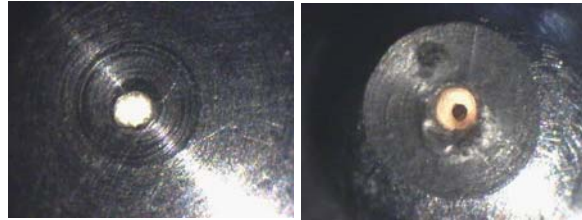


**Figure 8:** Aperture of 200  $\mu\text{m}$  diameter with a coaxial wire of 80  $\mu\text{m}$  thickness (right) and without a wire left).



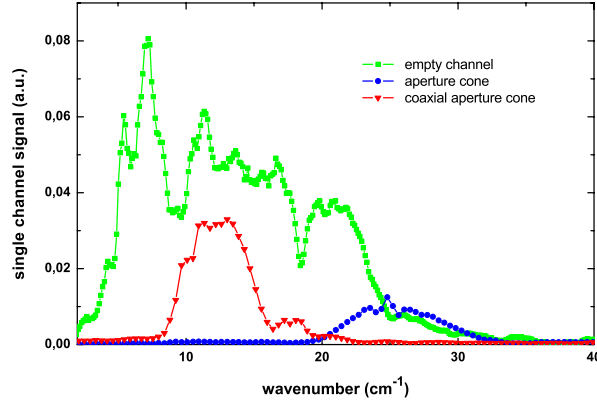


**Figure 9:** Single channel spectra of the empty spectrometer channel, of the aperture cone and of the coaxial aperture cone. The intensity of the empty channel spectra is attenuated by a factor of 100. Note, that the single channel intensities are shown in a linear scale.

Intensities through both cones are for wavenumbers down to  $2 \text{ cm}^{-1}$ .

imaging in strongly absorbing samples since it discriminates intensity from the source against thermal background radiation emitted by the beamline, the sample itself and the environment. The image is generated by interpretation of the SNIM signal versus sample position relative to the cone axis.

Conical aperture probes with a cone angle of  $50^\circ$  with two different aperture diameters of 100 and  $200 \text{ }\mu\text{m}$  have been employed for our experiments. Similar near-field probes have been proposed by Keilmann [32]. The conical aperture probe drastically attenuates the free-space THz radiation for wavelengths longer than the cut-off wavelength,  $\lambda_c = 1.71 d_c$ , where  $d_c$  is the relevant cross-section diameter of the cone [33]. The power output of the near-field probe for a specific wavelength then depends on the cone angle and the diameter of the exit aperture [34]. To increase the transmitted power and to shift the transmittance to longer wavelengths we also tested coaxial wire cones as described by Keilmann [33] and which are known to have theoretically no cut-off behavior. Both apertures under investigation, with and without a coaxial wire, are shown in Fig. 8. Fig. 9 shows the single channel spectra of the incident THz beam and the THz beam transmitted through the cones. Since the measurements are performed at ambient atmosphere all single channel spectra presented show distinct water absorption bands which do not interfere with our discussion. As expected from the geometry of the cones the transmitted power is reduced by several orders of magnitude. The transmittance of the cone without the wire has its maximum in the higher frequency range at wavenumbers where the CSR source starts to emit radiation. For the coaxial cone with a wire also a cut-off is observed. However, the maximum transmission shifts to smaller wavenumbers, e.g. to longer wavelengths. In contrast to the cone without the wire the transmission is suppressed for larger wavenumbers, perhaps caused by an insufficient coupling of the plane wave to the cone in this frequency range.

The spatial resolution of the THz SNIM was investigated by scanning the edge of an aluminum film on a Si wafer along the near-field probe. We obtained a spatial resolution which is on the order of the diameter of the aperture. From the  $2\sigma$ -value of the Gaussian fit of the first derivative of the experimental data, the spatial resolution is estimated to be about  $130 \text{ }\mu\text{m}$  for the  $200 \text{ }\mu\text{m}$  aperture probe and can be improved to  $70 \text{ }\mu\text{m}$  using the  $100 \text{ }\mu\text{m}$  aperture probe shown in Fig. 10. Taking broad band near-field images the spectral center of gravity at

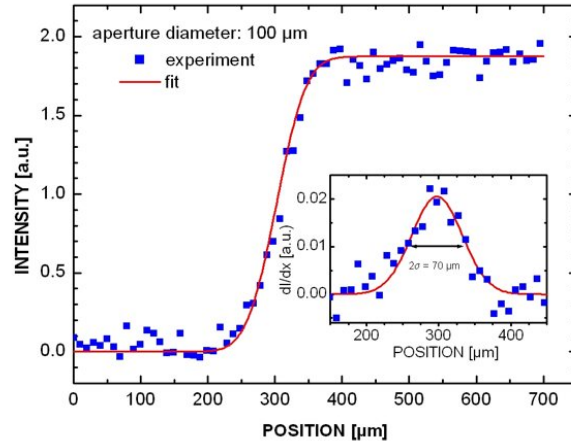


**Figure 10:** Measured and fitted spatial resolution curves for an exit aperture of 100  $\mu\text{m}$  diameter. The inset shows a Gaussian fit of the first derivative of the measured curve used to determine the spatial resolution.

around  $12\text{ cm}^{-1}$  is transmitted yielding an average spatial resolution of  $\lambda/6$  for the 200  $\mu\text{m}$  aperture and  $\lambda/12$  for the 100  $\mu\text{m}$  aperture, respectively.

The THz SNIM concept for applications on biological samples has been tested on leaves [8], where the contrast is mostly formed by the amount of liquid water present. Recently, images of living leaves have also been obtained by other authors [35, 36] from a confocal setup applying THz time-domain spectroscopy (TDS) to investigate the rehydration process of plants after watering. However, the spatial resolution of these investigations is restricted to the order of the wavelength applied. Using the THz SNIM technique presented here, much more detailed images can be obtained. Fig. 11 shows a part of a freshly cut *parthenocissus* leaf imaged in transmission. In its THz near-field image an inner structure of the veins is apparent which is mainly formed by liquid water absorption and possible scattering at the structural boundaries. Both the THz image and the visible light image reveal similar object features but the THz SNIM enables studies of hydration dynamics with a high spatial resolution because it is sensitive to the water concentration in the sample.

As initial tests of the feasibility of using sub-THz radiation in dentistry for the diagnosis of tooth decay, we have imaged human tooth material using the THz SNIM together with the coherent synchrotron radiation source at BESSY. If caries lesions are detected early enough, they can be arrested without the need for surgical intervention. X-ray imaging is a well established method to image human teeth. With this method, buried caries lesions can

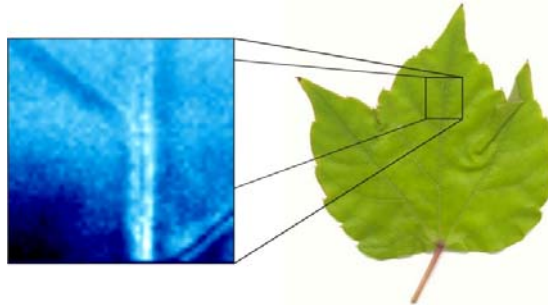


**Figure 11:** Near-field THz image (left) of a section of a *parthenocissus* leaf. Less absorption is indicated by a darker region in the THz image.

be imaged by a contrast change due to demineralization in the particular tooth region. However, the change in contrast is rather weak and only larger and strongly effected regions become visible in the x-ray image. Additionally, due to the ionizing nature of x-rays this method is not optimal for regular monitoring and many groups are exploring the infrared and THz radiation for medical imaging applications where both early diagnosis and safety issues are important. Recently, a more sensitive imaging method applying near infrared radiation was introduced [37], showing the potential to image early dental decay in the enamel. Tooth decay in the dentin could not be imaged by this method since the dentin is almost opaque in the near infrared. THz pulse imaging in the far infrared wavelength range has been performed for the detection of early stage caries in the enamel layer of thin (100  $\mu\text{m}$ ) human tooth cross sections [38] obtaining a higher attenuation of THz radiation in carious enamel as compared with healthy enamel. In contrast to the later confocal imaging investigation we applied the near-field technique and sub-THz radiation to image bulky tooth samples. Simulated buried caries lesions were produced by drilling 1-mm diameter cavity in the proximal region of the tooth and filling the cavity with hydroxyapatite paste [37] as shown in Fig. 12. The integral sub-THz image of the 2.7 mm thick tooth slab is shown in Fig.13 both for con-focal imaging and near-field imaging. The near-field image was obtained utilizing the 200- $\mu\text{m}$  wire cone while the confocal imaging was performed with the same optical set-up as shown in Fig. 7 except that the near-field cone was now removed. In confocal imaging geometry the tooth can not be spatially resolved and the image is strongly blurred as one would expect from diffraction due to the long wavelengths involved. In contrast the enamel and the dentin regions of the tooth sample as well as the simulated buried caries lesion together with other inner structural diversities are spatially resolved in the near-field image. Spectral near-field images have been obtained from the same sample. Fig. 14 shows a series of images of the

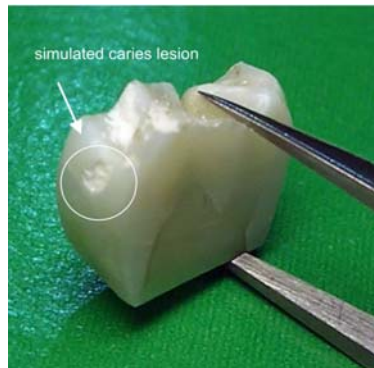


**Figure 12:** Photograph of a 2.7 m thick human tooth slab. The buried caries lesion is labeled on the left side.

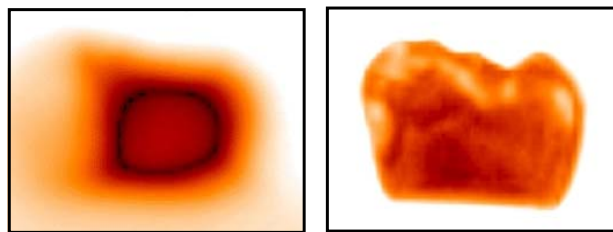


**Figure 13:** Confocal (left) and near-field (right) integral THz image of the tooth sample of Figure 12.

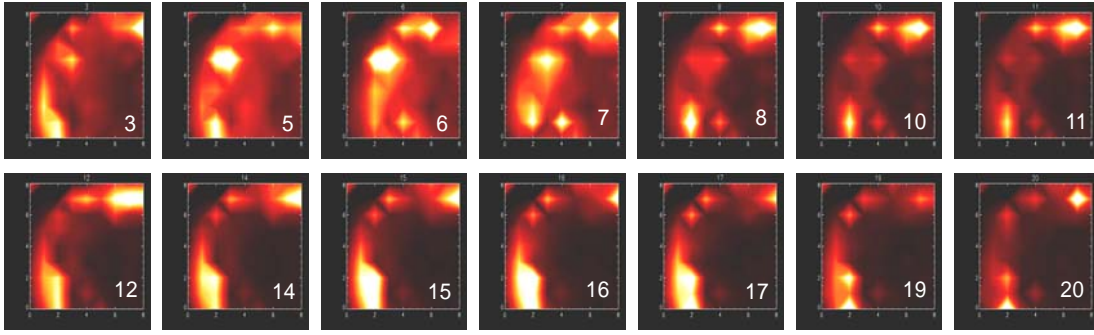


**Figure 14:** Series of spectral near-field images of the lesion region (upper left corner of the near-field image of Figure 12) between 3 and 20  $\text{cm}^{-1}$  (between 0.5 and 3 mm wavelength). The corresponding wavenumber is indicated on top of each spectral frame.

area with the simulated lesion for different wavenumbers. In the spectral band between 5 and 7 wavenumbers (2., 3. and 4. frame from left of the upper row in Fig. 14) the lesion is indicated by a lower attenuation of the sub-THz radiation in comparison to the absorption of the surrounding material. Whether this experimentally observed contrast is indicative for buried carious lesions in human teeth is still speculative and further investigations on the optical properties of tooth tissues and on the propagation of sub-THz radiation in inhomogeneous bulky samples have to be conducted.

These results on confining sub-THz radiation from an electron storage ring presented may have important implications for extending near-field applications to other imaging or spectroscopic applications in both life and material sciences.

### 1.1.5 Summary

The production of stable, high power, coherent synchrotron radiation at sub-terahertz frequency at the electron storage ring BESSY opens a new region in the electromagnetic spectrum to explore physical properties of materials. Just as conventional synchrotron radiation has been a boon to x-ray science, coherent synchrotron radiation may lead to many new innovations and discoveries in THz physics. With this new accelerator-based radiation source we have been able to extend traditional infrared measurements down into the experimentally poorly accessible sub-THz frequency range.

The feasibility of using the coherent synchrotron radiation in scientific applications was demonstrated in a series of experiments: We investigated shallow single acceptor transitions in stressed and unstressed Ge:Ga by means of photoconductance measurements below 1 THz. We have directly measured the Josephson plasma resonance in optimally doped  $\text{Bi}_2\text{Sr}_2\text{CaCu}_2\text{O}_8$  for the first time and finally we succeeded to confine the sub-THz radiation for spectral near-field imaging on biological samples such as leaves and human teeth.

### 1.1.6 References

1. Auston, D.H. et al., Phys. Rev. Lett **53** (1984), 1555.
2. Ferguson, B. and X.C. Zhang, Nature Materials **1** (2002), 26.
3. Abo-Bakr, M. et al., Phys. Rev. Lett, **88**25 (2002), 254801.
4. Carr, G.L. et al., Nature, **420** (2002), 153.

5. Abo-Bakr, M. et al., Phys. Rev. Lett. **90** (2003), 094801.
6. Wolf, J., Optical Engineering **33** (1994), 1492.
7. Singley E.J., et al., , Phys. Rev. B. **69** (2004), 092512.
8. Schade, U., et al., Appl. Phys. Lett. **84** (2004), 1422.
9. Haller, E. E., Infrared Phys. Technol. **35** (1994), 127.
10. Beeman, J. and Haller, E. E., Infrared Phys. Technol. **35** (1994), 827.
11. Kazanskii, A. G., et al., Appl. Phys. Lett. **3** (1977), 496.
12. Hasegawa, H., Phys. Rev. **129** (1963), 1029.
13. Schnurr, R., et al., Proc. of the Conf. on Infrared Astronomical Instrumentation SPIE **3354** (1998), 322.
14. Rabanus, D., et al., Proc. of the Conf on Airborne Telescope Systems, SPIE **4014** (2000), 137.
15. Kimmitt, M.F., et al., Proc. of the Conf. on Infrared Physics, (1988) 289.
16. Meny, C., et al., Proc. of the 15th Int. Conf. on Infrared and Millimeter Waves, (1990), 230.
17. Lax, M., Phys. Rev. **119** (1960), 1502.
18. Darken, L. S., Phys. Rev. Lett. **69** (1992), 2839.
19. Wilke, I., et al., Sol. State Comm. **93** (1995), 409.
20. Schade, U., et al., Rev. Sci. Instrum. **73** (2002), 1568.
21. Martin, D. H., and Puplett, E., Infrared Phys. **10** (1969), 105.
22. Landolt-Börnstein, New Series **II/22b** (1991), 480.
24. Anderson, P.W., *The theory of superconductivity in the high-T<sub>c</sub> cuprates*. Princeton series in physics. Princeton, N.J., Princeton University Press, 1997.
25. Dordevic, S.V., et al., Phys. Rev. B, **65** (2002), 134511.
26. Motohashi, T., et al., Phys. Rev. B, **61** (2000), R9269.
27. Tsui, O.K.C., et al., Phys. Rev. Lett. **73** (1994), 724.
28. The Drude model was used for the over damped plasmon with  $\omega_p = 895 \text{ cm}^{-1}$  and  $1/\tau = 8,000 \text{ cm}^{-1}$ .
29. Kakeshita, T., et al., Phys. Rev. Lett. **86** (2001), 4140.
30. Knoll, B., and Keilmann, F., Nature **399** (1999), 134.
31. Chen, H.-T., et al., Appl. Phys. Lett. **83** (2003), 3009.
32. Keilmann, F., U.S. Patent No. 4,994,818 (1991, filed 1989).
33. Keilmann, F., Infrared Phys. Technol. **36**, 217 (1995).
34. Knoll, B., and Keilmann, F., Opt. Commun. **162**, 177 (1999).
35. Mittelman, D., in *Sensing with Terahertz Radiation*, edited by D. Mittelman (Springer, Berlin, 2003), 137.
36. Koch, M., in *Sensing with Terahertz Radiation*, edited by D. Mittelman (Springer, Berlin, 2003), 303.
37. Jones, R.S., et al., Optics Express **11** (2003), 2259.
38. Crawley, D.A., et al., Caries Research **37** (2003), 352.